Received: 1 June 2023 | Revised: 20 December 2023 | Accepted: 30 December 2023

DOI: 10.1111/jace.19712

Journal of the American Ceramic Society

RESEARCH ARTICLE

A highly stable and conductive cerium-doped $Li_7P_3S_{11}$ glass-ceramic electrolyte for solid-state lithium–sulfur batteries

Amirhossein Mirtaleb[1,2] | **Ruigang Wang**[1,2]

[1]Department of Metallurgical and Materials Engineering, The University of Alabama, Tuscaloosa, Alabama, United States

[2]Department of Chemical Engineering and Materials Science, Michigan State University, East Lansing, Michigan, United States

Correspondence
Ruigang Wang, Department of Chemical Engineering and Materials Science, Michigan State University, East Lansing, Michigan 48824, United States.
Email: rwang@msu.edu

Funding information
Alabama Transportation Institute and Alabama Water Institute; National Science Foundation, Grant/Award Numbers: CBET-2118784, TI-2147564

Abstract

In this report, a facile wet chemical method using acetonitrile combined with thermal annealing was used to prepare Li_2S-P_2S_5 (LPS) based glass-ceramic electrolytes with (1 wt%, 3 wt%, and 5 wt% Ce_2S_3) and without Ce_2S_3 doping. The crystal structure, ionic conductivity, and chemical stability of $Li_7P_3S_{11}$ glass-ceramic electrolytes were examined at varying temperatures (250–350°C). The results indicated that the highest ionic conductivity of 3.15×10^{-4} S cm^{-1} for pure $Li_7P_3S_{11}$ was observed at a temperature of 325°C. By incorporating 1 wt% Ce_2S_3 and subjecting it to a heat treatment at 250°C, the glass ceramic electrolyte attained a remarkable ionic conductivity of 7.7×10^{-4} (S cm^{-1}) at 25°C. Furthermore, it exhibited a stable and extensive electrochemical potential range, reaching up to 5 volts when compared to the Li/Li^+ reference electrode. By tuning the glass transition and crystallization temperature, cerium doping seems to make $Li_7P_3S_{11}$ more chemically stable, compared to its original $70Li_2S$-$30P_2S_5$ counterpart. According to Raman and X-ray photoelectron spectroscopy analyses, cerium doping inhibits the decomposition of highly conductive $P_2S_7^{4-}$ (pyro-thiophosphate) to PS_4^{3-} and $P_2S_6^{4-}$. Doped LPS has a greater crystallinity and more uniform microstructure than pure LPS, according to XRD, Raman spectroscopy, and scanning electron microscopy analysis. Consequently, $Li_7P_{2.9}Ce_{0.1}S_{11}$ electrolyte shows great potential as a solid-state electrolyte for constructing high-performance sulfide-based all-solid-state batteries.

KEYWORDS
cerium doping, ionic conductivity, $Li_7P_3S_{11}$ glass ceramic, solid-state electrolyte

1 | INTRODUCTION

Energy storage devices have been extensively researched due to the depletion of fossil fuels, global warming, wide usage of renewable energy, and the growing energy demand.[1–3] Currently, the systems of convectional energy allocation and production are under strain. To meet the growing energy demand, energy storage devices with superior energy density, thermal/electrochemical stability, and sustainable/cost-effective materials must be developed urgently. Besides storing energy from intermittent renewable sources such as solar, wind, and hydropower, these devices can also store energy from traditional sources such as coal and natural gas. In the event of a power outage, this stored energy can then be used to meet peak demand. Additionally, energy storage devices can reduce

the cost of energy production and distribution.[4,5] Energy storage devices reduce energy production and distribution costs by storing energy when it is abundant and inexpensive and then releasing it when needed. Furthermore, energy storage devices can reduce energy production's environmental impact.[6] Carbon dioxide and other pollutants (including greenhouse gases) are reduced in the atmosphere when energy storage devices store energy from renewable sources.[7,8] In this way, global warming and other environmental problems can be mitigated. Currently, lithium-ion battery is undeniably one of the greatest triumphs of modern electrochemistry storage devices due to its high single-cell voltage, lack of memory effect, long cycle life, and high energy density. Portable electronics have enabled small-scale energy storage (by the Wh) to achieve unprecedented success.[9–14]

According to some experimental evidence, liquid organic electrolytes are a contributing factor to the potential hazards due to thermal runaway associated with lithium-ion batteries. Thus, much effort is being put into developing thermally/electrochemically stable electrolytes capable of withstanding higher temperature and providing high performance.

In light of this, solid-state electrolytes have gained considerable attention and have gained prominence. A solid-state electrolyte is a material capable of conducting ions, such as lithium or other charge-transfer ions.[15,16] Their substance is usually ceramic, polymer, or composites, which make them much more thermally stable than liquid electrolytes. Their non-flammability and lack of leakage also make them safer. Additionally, solid-state electrolytes have a higher cycle life as well as fewer packaging and state-of-charge monitoring requirements.[17] In contrast to oxides and phosphates, solid-state electrolytes based on sulfide have generally higher ionic conductivities in the range of 10^{-4} to 10^{-2} S cm^{-1} than those based on oxides and phosphates. In comparison with oxygen, sulfur has a larger ionic radius, and its electronegativity is also weaker than oxygen. As a result, sulfur compounds have longer bond length. In addition, the bond strength is weaker than that of oxides. As they have a wider diffusion path, they can achieve higher ionic conductivity, making them a suitable alternative to liquid electrolytes.[18] For example, Kato et al.[19] report that the unique structure of $Li_{10}GeP_2S_{12}$ can have an exceptionally high lithium ionic conductivity of $> 1 \times 10^{-2}$ S cm^{-1}. Typically, sulfides are also softer and more flexible than oxides and phosphates because of their lower elastic moduli. They are, therefore, easier to work with and less likely to damage battery components during production. Additionally, sulfide-based solid-state electrolytes are more compatible with current battery production processes, so manufacturers can switch to sulfide-based electrolytes without having to make significant changes to their manufacturing processes.[20–26]

Some sulfide systems have ionic conductivity that exceeds that of liquid electrolytes. Glass ceramics such as $Li_7P_3S_{11}$ are notable examples. The $Li_7P_3S_{11}$ electrolyte plays a crucial role in advancing all-solid-state batteries, offering a promising alternative to traditional lithium-ion batteries. This unique electrolyte material provides several advantages, including improved safety, enhanced stability, and increased energy density. By substituting liquid electrolytes with solid-state counterparts, the risks associated with leakage, flammability, and thermal runaway are significantly reduced.[27] $Li_7P_3S_{11}$ is a solid-state electrolyte composed of lithium (Li), phosphorus (P), and sulfur (S), and it possesses a distinctive crystal structure that enables efficient transport of lithium ions while maintaining chemical stability. The high concentration of lithium ions within the structure promotes rapid ion conduction, positively impacting the overall performance of the battery.[28]

One notable benefit of $Li_7P_3S_{11}$ is its strong stability against lithium metal, effectively preventing the formation of dendrites. Dendrites are needle-like structures that can form during battery charge–discharge cycles and pose risks such as short circuits and reduced battery lifespan. The stability provided by $Li_7P_3S_{11}$ significantly contributes to the longevity and reliability of the battery. Furthermore, $Li_7P_3S_{11}$ exhibits a wide electrochemical stability range, allowing for operation at higher voltages without compromising integrity. This characteristic enables the utilization of high-capacity electrode materials, resulting in increased energy density and extended battery lifespan.[29] Mizuno et al.[30] synthesized the $Li_7P_3S_{11}$ glass-ceramic solid-state electrolyte composed of $70Li_2S{\cdot}30P_2S_5$ (mol%) for the first time. Then Yamane et al.[31] found that metastable $Li_7P_3S_{11}$ and Li_3PS_4 have conductivities of 3×10^{-3} and 1.6×10^{-4} S cm^{-1}, respectively. Compared with ceramic matrix, Li^+ ions are more mobile within the glass matrix, which may contribute to their high ionic conductivity. Li^+ ions can more freely move through the glass matrix, allowing efficient charge transport. Several factors determine ionic transport in solid-state (inorganic) electrolytes, including mobile ions and vacancies, ion diffusion properties at grain boundaries, and the size of connected conduction pathways in crystal structures with Schottky and Frenkel point defects.[32] There are three primary groups of techniques for synthesizing sulfide-based solid-state electrolytes: solid reaction methods, mechanochemical reaction methods, and wet chemical methods. Wet chemical methods are considered as one of the most effective ways for producing nanosized solid-state electrolytes because they allow for a uniform blend with the cathodic electrode. Additionally, wet chemical methods are well-suited for large-scale

synthesis and manufacture, especially at lower reaction temperatures.[33,34]

Additionally, numerous studies are currently being conducted on the materials for dopants, which could significantly impact ionic conductivity and battery performance. It seems that adding dopants to $Li_7P_3S_{11}$ has a more significant effect on ionic conductivity. As a result of doping the sulfide electrolytes system, not only would point defects be produced but also a broader range of defect kinds and concentration would be generated or manipulated. Channels of lithium-ion transfer may be created and contribute to the ionic conductivity of solid-state electrolytes. By doing so, electrodes and solid-state electrolytes will exhibit lower interfacial resistance, leading to better performance at high rates. Also, solid-state electrolytes can be more chemically stable, preventing from decomposing and allowing the use of high-voltage Li cathode materials, and their working voltage ranges can be extended between 0.5 and 5 V.[23,29,35–48] Among various dopants, cerium (Ce) or CeO_{2-x} has received considerable attention in the research community. There are several advantages associated with cerium doping, including an increased ionic conductivity, improved stability, and a suppression of the polysulfide shuttle effect in Li-S battery. The cerium ions (Ce^{4+}/Ce^{3+}) can act both as redox mediators and as redox catalysts in Li-S battery due to their variable oxidation states. As a result, they can immobilize and convert polysulfides, thus reducing their migration and alleviating capacity degradation.[45,46,49] When cerium is introduced into Li_2S-P_2S_5 (LPS), the defect structure and/or conentration of the material can be modified, thereby enhancing the migration of Li^+ ions, resulting in an improvement in the ionic conductivity of the material. It is believed that a significant part of this enhancement can be attributed to the introduction of additional mobile charge carriers and the optimization of the Li-ion diffusion pathways.[47,48] Researchers have studied the effect of cerium doping in the cathode of Li-S battery, but rarely have they examined doping the $Li_7P_3S_{11}$ solid-state electrolyte with cerium sulfide.

In this report, by doping $Li_7P_3S_{11}$ with cerium sulfide, we aim to improve its chemical stability and ionic conductivity. A glass-ceramic electrolyte with Ce doping (1 wt%, 3 wt%, and 5 wt% Ce_2S_3) in Li_2S–P_2S_5 using a wet chemical route was designed and fabricated. Using a precipitation method, $Li_7P_{2.9}Ce_{0.1}S_{11}$ nanopowders were synthesized and then pressed into pellets as an electrolyte. By incorporating 1 wt% Ce_2S_3 into the material and subjecting it to a heat treatment at 250°C, the glass-ceramic electrolyte demonstrated an impressive ionic conductivity of 7.7×10^{-4} S cm^{-1} at 25°C. Furthermore, it exhibited a consistent and wide electrochemical potential range, extending up to 5 volts, compared to the Li/Li^+ reference electrode. The addition of Ce_2S_3 contributes to the thermal stability of $Li_7P_3S_{11}$ during heating through influencing the glass transition and crystallization temperature. Raman and X-ray photoelectron spectroscopy (XPS) analyses indicate that Ce_2S_3 hinders the decomposition of $P_2S_7^{4-}$ (which possesses high ionic conductivity) into PS_4^{3-} and $P_2S_6^{4-}$. Electron microscopy analysis also suggests that the doped LPS has a higher degree of crystallinity, compared to pure LPS. These findings suggest that the $Li_7P_{2.9}Ce_{0.1}S_{11}$ electrolyte holds great potential for utilization as a solid-state electrolyte in high-performance all-solid-state Li-S batteries.

2 | EXPERIMENTAL PROCEDURES

2.1 | Material synthesis

Ce_2S_3 (99.9%, Thermo Scientific) with a 1 wt%, 3 wt% and 5 wt% loading was mixed with Li_2S (99.9%, Alfa Aesar) and P_2S_5 (99.9%, Sigma-Aldrich; 7:3 molar ratio) in acetonitrile (anhydrous, 99.8+%, Thermo Scientific) solvent under stirring at 50°C for 72 h; then, the suspension was filtered, and dried in a vacuum oven at 60°C for 24 h. After that, the obtained powder was ground and heated under an inert atmosphere of argon for 2 h to obtain the electrolyte. Heat treatment temperature was varied from 250 to 350°C to understand the crystallinity–ionic conductivity relationship of the sulfide solid-state electrolytes. Thereafter, the powders were pressed with 360 MPa in a glove box to obtain pellets used in assembling solid-state electrolytes. The pure phase $Li_7P_3S_{11}$ (ICSD#157654) was obtained after annealing at 250°C for 2 h. According to the literature, when the annealing temperature is too high, an impurity phase of $Li_4P_2S_6$ (ICSD#80319) forms, which has a much lower ionic conductivity (10^{-7} S cm^{-1}),[50] while $Li_7P_3S_{11}$ is difficult to crystallize at a low heat-treatment temperature. The preparations were carried out in an argon atmosphere with a water and oxygen content of less than 0.1 parts per million in glove box. In the absence of Ce_2S_3, $Li_7P_3S_{11}$ electrolyte was synthesized using the same method as mentioned above (Figure 1).

2.2 | Material characterization

An X-ray diffractometer (Philips X'Pert MPD) with Cu Ka radiation (k = 1.5405 Å) operated at 45 kV, and 40 mA was used for determining the crystal structure while the powder sample was held on a zero-background quartz sample holder. An angular movement was supported by a goniometer, resulting in X-ray data in the range of 10° to 60° with a controlled step size of 0.5°min^{-1}.

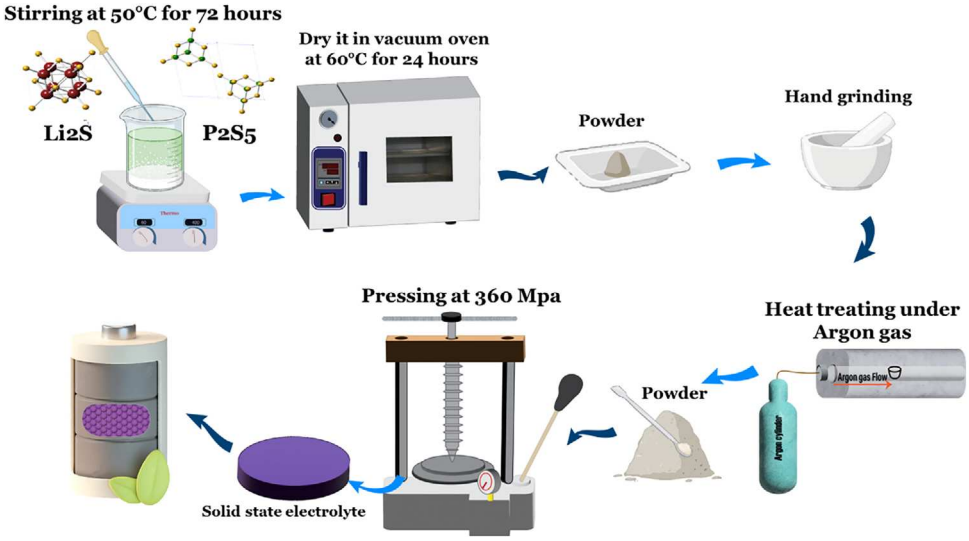

FIGURE 1 Schematic diagram of the synthesis procedures for $Li_7P_{2.9}Ce_{0.1}S_{11}$ glass ceramic.

HighScore Plus software equipped with the JCPDS-JCDD database was used to index peak positions. Raman spectroscopy was carried out using a Horiba Lab-RAM HR 800 Raman spectrometer equipped with a wide spectral window (100~1200 cm^{-1}) and a 100 long-working-distance objective (NA = 0.60). Calibration of the Raman spectrometer was performed on a single-crystal silicon wafer (520.7 cm^{-1}).

XPS was employed by using a Versa Probe 5000 spectrometer with monochromatic Al Kα (hν = 1486.6 eV) radiation at a working pressure of $< 8 \times 10^{-10}$ Torr. The carbon C 1s line (284.8 eV) was used as a reference for standard calibration. Scanning electron microscopy (SEM) images were collected using Thermo Scientific Apreo FE-SEM with an accelerated voltage ranging from 1 to 30 kV. Additionally, the instrument is equipped with Energy Dispersive X-ray Analysis (EDAX) for performing Energy Dispersive X-ray Spectroscopy (EDS) with elemental mapping and data processing software APEX-EDS. To characterize the thermal stability and decomposition temperature of $Li_7P_3S_{11}$ powders, a STA8000 simultaneous thermogravimetric analysis/differential scanning calorimetry (TGA/DSC) Analyzer (PerkinElmer Inc.) was used. Samples (30 mg) were loaded into alumina crucibles and ramped from room temperature to 1000°C at a heating rate of 10°C min^{-1} under a constant flow of N_2 at 20 mL min^{-1}.

2.3 | Electrochemical measurements

Electrochemical impedance spectroscopy (EIS) was used to measure the ionic conductivities of the synthesized $Li_7P_3S_{11}$ and $Li_7P_{2.9}Ce_{0.1}S_{11}$ electrolytes. The electrolyte pellets were produced with a thickness of 0.7 mm and a diameter of 14.85 mm under a pressure of 360 MPa. These solid-state electrolyte pellets were sandwiched with stainless steel foils. EIS measurements were conducted using a Gamry Potentiostat/Galvanostat workstation (Gamry Interface 1000E). Each electrochemical measurement was conducted at a temperature of 25°C. The ionic conductivity σ_{Li+} (S cm^{-1}) of the electrolytes was measured by the equation given below.

$$\sigma_{Li+} = d/(S \times R_{total}), \quad (1)$$

where R is the resistance value, d is the pellet thickness and S is the pellet cross-sectional area.

3 | RESULTS AND DISCUSSION

3.1 | Structural characterization

The effects of dopants and heat-treating temperature on the structure and properties of sulfide electrolytes synthesized by acetonitrile were investigated. The results showed that the Ce_2S_3 doping significantly altered the structure and properties of the sulfide electrolytes. The X-ray diffraction (XRD) patterns of the $Li_7P_3S_{11}$ and $Li_7P_{2.9}Ce_{0.1}S_{11}$ solid-state electrolytes heated at 250, 275, and 300°C are shown in Figure 2.

As is clear in the XRD patterns, $Li_7P_3S_{11}$ shows an amorphous structure with broad diffraction peaks for the samples treated at 250 or 275°C, while the sample treated at 300°C presents better crystallinity. By increasing the heat treatment temperature from 250 to 300°C, the content of amorphous structure reduces. As Figure S1 shows, through raising the heat treatment temperature

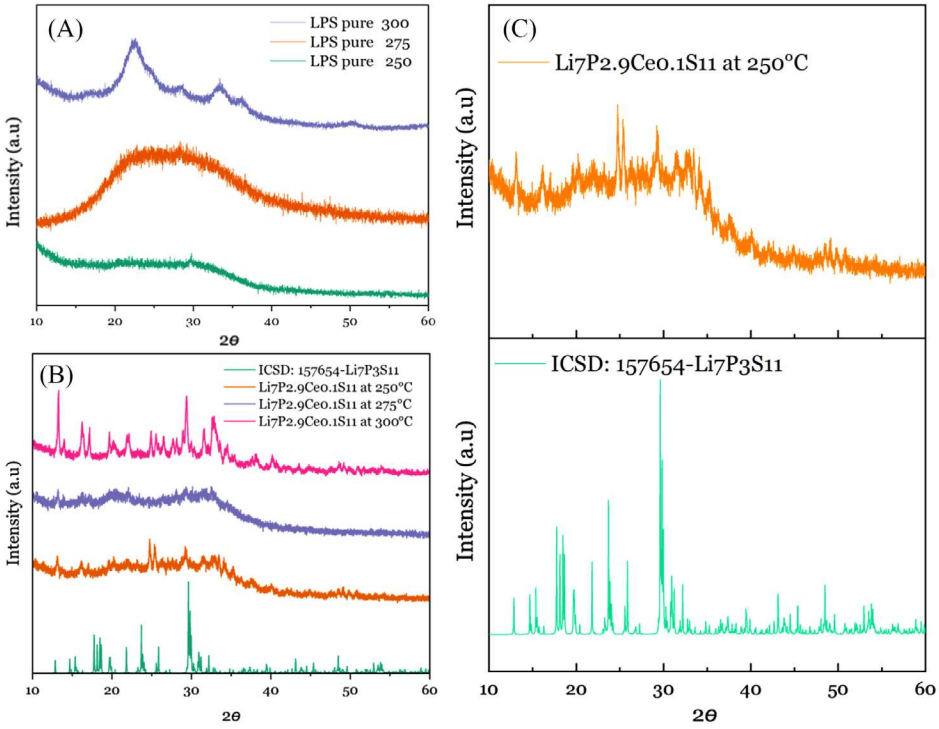

FIGURE 2 The XRD patterns for (A) $Li_7P_3S_{11}$ and (B) $Li_7P_{2.9}Ce_{0.1}S_{11}$ glass ceramics treated at different temperatures. (C) Comparison of XRD patterns between the synthesized $Li_7P_{2.9}Ce_{0.1}S_{11}$ glass ceramic at 250°C and standard PDF card.

from 250 to 325°C, a great number of peaks can be observed in the $Li_7P_3S_{11}$ sample. Furthermore, when the temperature was further increased to 350°C, there was a noticeable phase transformation from $Li_7P_3S_{11}$ to $Li_4P_2S_6$. This transition results in a lower ionic conductivity for the latter compound.[50] While $Li_7P_{2.9}Ce_{0.1}S_{11}$ remains virtually unchanged during heating, it displays a crystal structure at the temperature of 250°C. Moreover, Figure S2 illustrates that LPS containing 1 wt% Ce_2S_3 exhibits a mixture of glassy and crystalline phase characteristics at 250°C. The XRD patterns display similar phase identification results when cerium is added at 3 wt% and 5 wt%.

In the XRD patterns, it can be determined that the diffraction peaks at 20.3, 24.8, 25.5, 29.7, and 33.5° belong to $Li_7P_3S_{11}$ (ICDS# 157654).[51] In this study, it was found that a small amount of Ce_2S_3 doping (1 wt%) can significantly enhance the crystal nucleation rate to a significant extent. Moreover, no new crystalline phases related to Ce were detected in the $Li_7P_{2.9}Ce_{0.1}S_{11}$ matrix, which implies that Ce ions exist either at a substitutional position or in the glass phase in the LPS matrix. If Ce^{3+} substitutes Li^+ or P^{5+}, due to the charge difference (Ce^{3+} in Ce_2S_3; Li^+, P^{5+}, and S^{2-} in $Li_7P_3S_{11}$), it is expected that various defects can be generated, and channels of lithium transmission are widened (ionic size for Ce^{3+}: 1.07 Å and ionic size for P^{5+}: 0.38 Å, which could promote the transport of lithium ions and further enhancing ionic conductivity.[38]

3.2 | Thermogravimetric analysis

At elevated temperatures, as a result of the precipitation of thermodynamically stable crystalline phases from a parent glass, grain-boundary resistance cae reduced to a great extent. There are several possible reasons for the reduction in grain-boundary resistance during devitrification: the crytalline phases have well-defined atomic arrangements, whereas the glasses lack long-range order. As crystalline grains form, atomic structures become higher ordered than in the original glass due to the formation of grain boundaries. Improved atomic ordering can result in better atomic connectivity across grain boundaries, reducing ion transport resistance. Moreover, grain-boundary mobility is enhanced during devitrification due to the rearrangement of atoms and migration of grain boundaries. At elevated temperatures, grain boundaries become more mobile, allowing atoms to rearrange and defects to disappear and/or regroup. Enhancing mobility can reduce grain-boundary resistance. in addition, in glass, amorphous phases can introduce structural defects and irregularities at grain boundaries, hindering ion carrier movement. In devitrification, the amorphous phase transforms into crystalline phases, eliminating structural defects and resulting in smoother grain boundaries. A smoother grain boundary facilitates the flow of ion carriers and reduces resistance.[52,53]

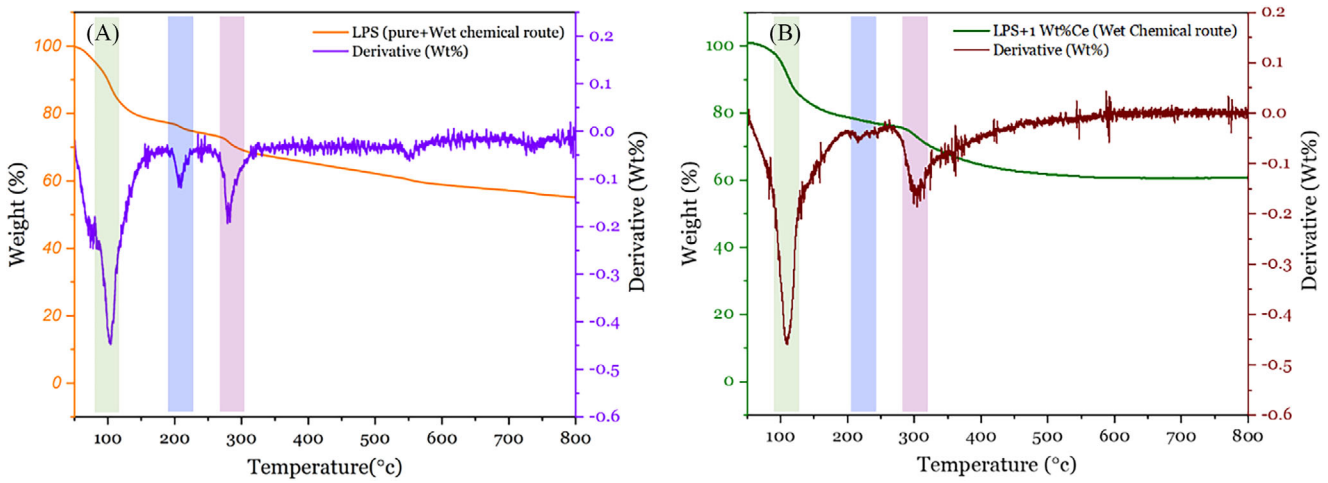

FIGURE 3 The TGA and DTG curves for (A) $Li_7P_3S_{11}$ and (B) $Li_7P_{2.9}Ce_{0.1}S_{11}$.

TGA and derivative thermogravimetry (DTG) (Figure 3) show that both samples have a significant thermal event around 100°C. On close inspection, the peak and onset temperatures of the $Li_7P_{2.9}Ce_{0.1}S_{11}$ sample differ by 5~24°C from the $Li_7P_3S_{11}$ sample (108 vs. 103°C, 216 vs. 205°C, and 303 vs. 279°C).

As a result of the heating, both samples lose a significant amount of weight below 200°C. An unknown crystalline phase was reported by Rangasamy et al.[54,55] formed when Li_2S and P_2S_5 were combined with acetonitrile at a 3:1 molar ratio. This weight loss can be attributed to acetonitrile absorption below 200°C for the sample.[29,34,55]

A smooth continuous trend is evident throughout the temperature range in the TG and DTG curves of the samples. In addition, examing the graphs more closely, at around 220°C, the baseline shift indicates that the material underwent a glass transition. Further heating of the samples produced a change in baseline measurement and a shift in crystallization temperature (Tc) around 290°C. $Li_7P_{2.9}Ce_{0.1}S_{11}$ has a significantly lower glass transition and crystallization temperature than those of $Li_7P_3S_{11}$. The result can be attributed to the fact that cerium changes the glass transition temperature and makes $Li_7P_3S_{11}$ more stable. It is clear that the addition of Ce_2S_3 affected the growth rate and nucleation of $Li_7P_3S_{11}$.

3.3 | XPS analysis

XPS was used to determine the surface ionic bonding or coordination environment in undoped and doped LPS. In $Li_7P_3S_{11}$ and $Li_7P_{2.9}Ce_{0.1}S_{11}$, different anionic polyhedral can be distinguished by three-bridging sulfur (P-S-P) aligned with neighboring PS_4^{3-} tetrahedral (non-bridging sulfur). An XPS spectrum can be used to distinguish between the bridging (P-S-P) and terminal (P-S-Li) sulfurs in di-tetrahedral $P_2S_7^{4-}$ anion. The XPS spectra for $Li_7P_{2.9}Ce_{0.1}S_{11}$ and $Li_7P_3S_{11}$ are shown in Figure 4. Through spin-orbital splitting, the S 2p signals can be divided into two parts: S $2p_{1/2}$ and S $2p_{3/2}$. In the as-prepared glass-ceramic, three different kinds of sulfur species can be distinguished. The XPS spectrum of $Li_7P_3S_{11}$ shows one bridging sulfur bonding to the phosphorus atom in PS_4^{3-} (P = S) at 161.6 eV and one non-bridging sulfur bonding to the phosphorus atom (P-S-Li) at 160.38 eV. The XPS analysis of $Li_7P_{2.9}Ce_{0.1}S_{11}$ revealed the presence of di-tetrahedra $P_2S_7^{4-}$ (P-S-P) and tetrahedra PS_4^{3-} (P = S) at 162.5 and 161.2 eV, respectively. A non-bridging sulfur bond (P-S-Li) was also observed at 160.2 eV.[48,51,55–57]

Spin-orbit coupling of the electrons in the P 2p orbital causes the spin-orbit splitting of the P 2p signal. Electrons are coupled because of the interaction between their spin and orbital angular momentum. As a result of the different energies of the two spin-orbit components of the P 2p orbital, the P 2p signal spin-orbit splits. Orthothiophosphate signals are associated with higher energy components, while pyro-thiophosphate signals are associated with lower energy components. $Li_7P_3S_{11}$ showed two responsive peaks at 131.4 and 132.1 eV corresponding to the $P_2S_7^{4-}$ di-tetrahedral unit and one at 132.8 eV corresponding to the PS_4^{3-} tetrahedral unit. As with $Li_7P_{2.9}Ce_{0.1}S_{11}$, the di-tetrahedral unit $P_2S_7^{4-}$ was observed at 130.7 and 131.9 eV, and the tetrahedral unit PS_4^{3-} was seen at 132.9 eV, confirming the classification of new doped glass-ceramic electrolytes as $Li_7P_3S_{11}$. As far as we can tell, we have not been able to find any peaks related to Ce 3d bonding in XPS data.

Data from XRD and impedance spectroscopy indicate that Li-ion conductivity is highly correlated in $Li_7P_3S_{11}$'s structure. However, the Li-ion conductivity difference in structure cannot fully be explained. The Raman spectroscopy data of $Li_7P_3S_{11}$ glass-ceramic provide the

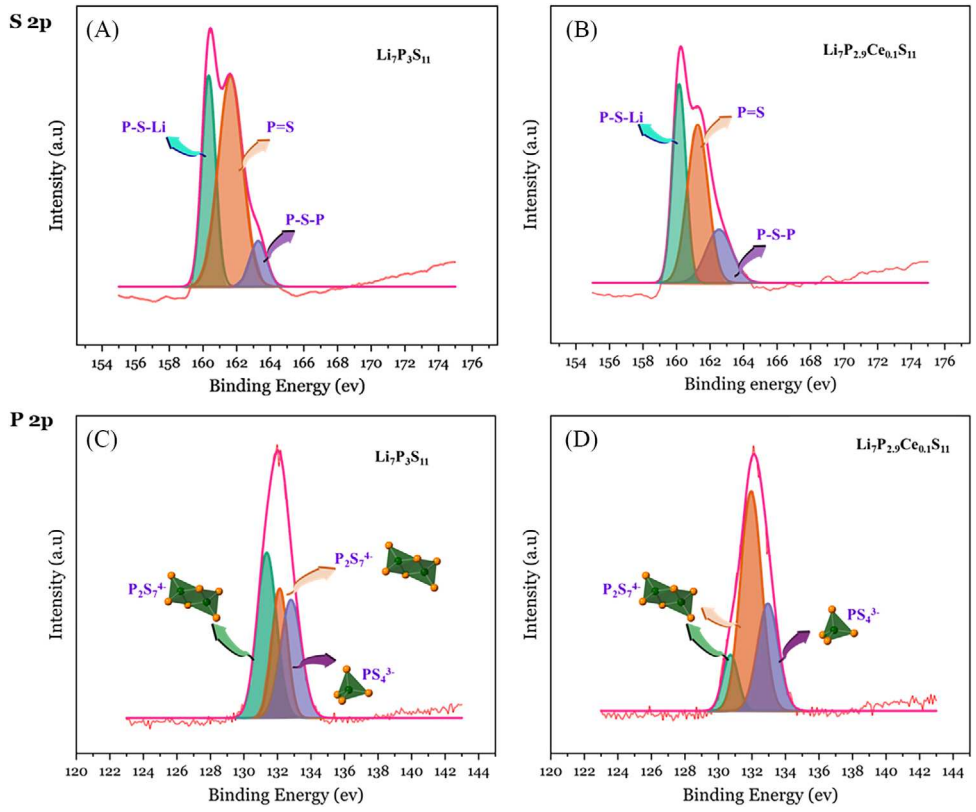

FIGURE 4 Deconvoluted X-ray photoelectron spectra: (A) S 2p for $Li_7P_3S_{11}$; (B) S 2p for $Li_7P_{2.9}Ce_{0.1}S_{11}$; (C) P 2p for $Li_7P_3S_{11}$; and (D) P 2p for $Li_7P_{2.9}Ce_{0.1}S_{11}$.

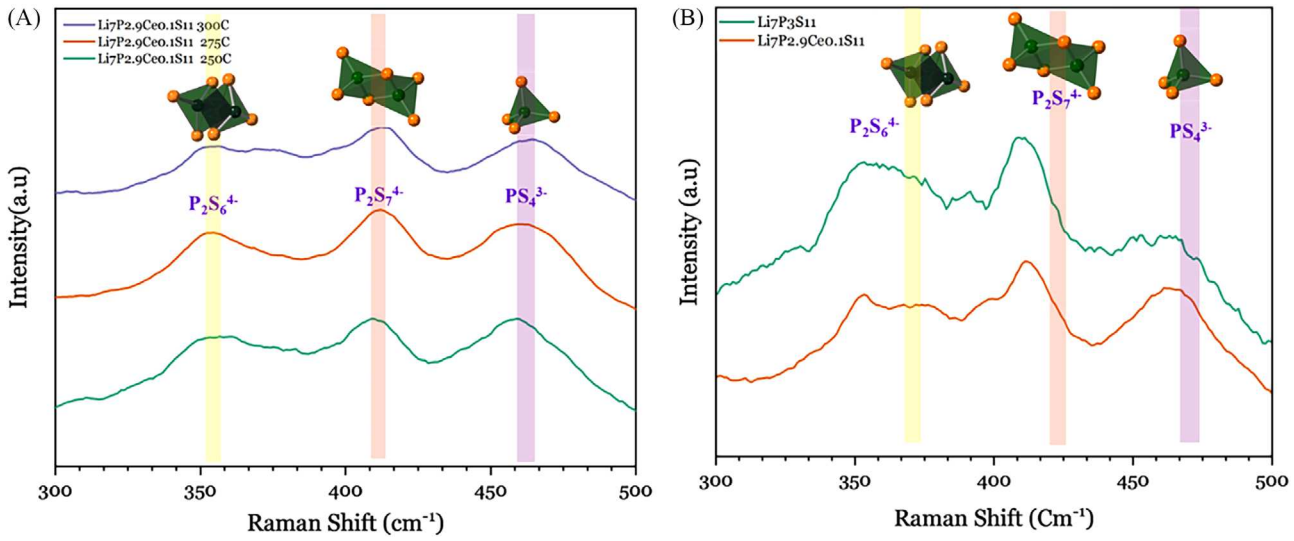

FIGURE 5 Raman spectra of (A) $Li_7P_{2.9}Ce_{0.1}S_{11}$ heat treated at 250, 275, and 300°C and (B) $Li_7P_3S_{11}$ and $Li_7P_{2.9}Ce_{0.1}S_{11}$.

explanation instead. Raman spectroscopy was used to measure the effects of cerium doping on the coordination environments of the PS_x ion clusters. According to Figure 5, $Li_7P_{2.9}Ce_{0.1}S_{11}$ glass-ceramic electrolyte shows three main peaks at 352, 411, and 459 cm^{-1}, corresponding to $P_2S_6^{4-}$ ions, $P_2S_7^{4-}$ ions, and PS_4^{3-} ions. These three peaks remain virtually unchanged during the heat treatment from 250 to 300°C, whereas for $Li_7P_3S_{11}$, this peak shifts during heating. In addition, the $Li_7P_3S_{11}$and $Li_7P_{2.9}Ce_{0.1}S_{11}$ Raman spectroscopy data illustrate that

intensity and ratio of $P_2S_6^{4-}$ ion in $Li_7P_3S_{11}$ are higher than those in $Li_7P_{2.9}Ce_{0.1}S_{11}$. It has been reported that the $P_2S_6^{4-}$ cluster leads to lower ionic conductivity, while the $P_2S_7^{4-}$ cluster contributes to higher ionic conductivity. In $P_2S_6^{4-}$, two phosphorus atoms are grouped with six sulfur atoms, while in $P_2S_7^{4-}$, two phosphorus atoms are grouped with seven sulfur atoms. The difference in ionic conductivity between the two clusters is probably due to the different number of sulfur atoms. $P_2S_7^{4-}$ has a higher ionic conductivity due to its high sulfur content, which increases the number of pathways for ionic conduction. These results indicate that Li-ion conductivity is higher when $P_2S_7^{4-}$ and PS_4^{3-} are present.[58] In order for lithium ions to conduct quickly, there must be many interstitial sites between $P_2S_7^{4-}$ ditetrahedra and PS_4^{3-} tetrahedra in the structure of $Li_7P_3S_{11}$.[31] Furthermore, the presence of $P_2S_7^{4-}$ and PS_4^{3-} peaks is associated with higher Li-ion diffusion coefficients, indicating that these peaks are important for Li-ion transport. In addition, there is a possibility that, as temperature increases, the presence of cerium inhibits the dissociation of $P_2S_7^{4-}$ to PS_3^- and PS_4^{3-}.

3.4 | Morphology

Figure 6 illustrates how the $Li_7P_3S_{11}$ and $Li_7P_{2.9}Ce_{0.1}S_{11}$ powders have a variety of shapes and particle sizes based on their SEM images. The particle morphology and size of the synthesized $Li_7P_3S_{11}$ were also compared for the samples treated from 250 to 350°C in Figure S3. These figures clearly demonstrate the transition from less crystalline powders to crystallized powders when the heat treatment temperature increases. According to the XRD patterns, the crystallinity of $Li_7P_3S_{11}$ glass powder increases with the increasing temperature of heat treatment. In spite of this, $Li_7P_{2.9}Ce_{0.1}S_{11}$ exhibits a higher crystallinity, compared with $Li_7P_3S_{11}$. The uniform dispersion of P and S in the synthesized powders can also be observed in Figure 6. The EDS analysis revealed that the elements in question are uniformly distributed on the powder surface, showcasing a homogeneous mixing. Figure S4 illustrates the structure and appearance of the produced $Li_7P_3S_{11}$ with varying compositions of Ce_2S_3, namely, 1 wt%, 3 wt%, and 5 wt%. The results indicate a noticeable decrease in particle size as the doping level changes from 1 wt % to 5 wt%.

3.5 | Ionic conductivity

The Arrhenius conductivity plot was used to determine the ionic conductivity of $Li_7P_3S_{11}$ and $Li_7P_{2.9}Ce_{0.1}S_{11}$ at room temperature. The highest ionic conductivity of $Li_7P_3S_{11}$ was 3.15×10^{-4} S cm^{-1} at room temperature, which is comparable to the results reported in the previous literature[59] and cerium-doped electrolyte, $Li_7P_{2.9}Ce_{0.1}S_{11}$, which exhibited a higher ionic conductivity of 7.7×10^{-4} S cm^{-1} at 250°C (Table 1 and 2).

TABLE 1 Lithium thiophosphates bond positions and visualization.

Modes	Lithium Thiophosphates		
	$P_2S_6^{4-}$	$P_2S_7^{4-}$	PS_4^{3-}
Wavenumber/cm^{-1}	352	411	459
Visualization	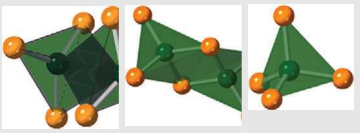		

As shown in Figure 7, it is clear that $Li_7P_{2.9}Ce_{0.1}S_{11}$, after being heat-treated at different temperatures, has a higher ionic conductivity than $Li_7P_3S_{11}$ at all stages of the heat treatment process. It is possible that the higher ionic conductivity of doped $Li_7P_3S_{11}$ is closely related to the crystallinity and the relative concentration of various $P_xS_y^{z-}$ groups of the glass ceramic. XRD and Raman tests have shown that the $Li_7P_{2.9}Ce_{0.1}S_{11}$ samples have a higher degree of crystallinity than $Li_7P_3S_{11}$, and the ratio of the $P_2S_7^{4-}/PS_4^{3-}$ is also higher in $Li_7P_{2.9}Ce_{0.1}S_{11}$. It can be seen from Figure 7 and Table 2 that the effect of the heat treatment on the ionic conductivity of $Li_7P_{2.9}Ce_{0.1}S_{11}$ is less than that of $Li_7P_3S_{11}$ at different temperatures, demonstrating better thermal stability for $Li_7P_{2.9}Ce_{0.1}S_{11}$. Based on the data in Table 2, the highest ionic conductivity in $Li_7P_3S_{11}$ is attributed to the sample treated at 325°C. Based on the data provided in Figure S5 and Table 2, it was observed that raising the heat treatment temperature from 250 to 325°C had a positive impact on the ionic conductivity of $Li_7P_3S_{11}$, leading to an increase in conductivity and a decrease in total resistance. However, beyond 325°C, at a heat treatment temperature of 350°C, the ionic conductivity of $Li_7P_3S_{11}$ started to decline. It is most likely that the decrease in ionic conductivity at a temperature higher than 325°C is related to the formation of $Li_4P_2S_6$, a less conductive phase. From Figure S6 and Table 2, there is a slight decrease in the ionic conductivity of the doped $Li_7P_3S_{11}$ as the amount of Ce_2S_3 dopant increases from 1 wt% to 5 wt%. However, all the conductivity values remain at the level of 10^{-4} S cm^{-1}.

3.6 | Cyclic voltammetry (CV)

The CV curves depicted in Figure 8A,B showcase the results obtained from conducting CV on asymmetric Li/solid electrolyte/stainless steel cells using two different electrolytes: $Li_7P_3S_{11}$ and $Li_7P_{2.9}Ce_{0.1}S_{11}$. These measurements were performed at room temperature with a scan

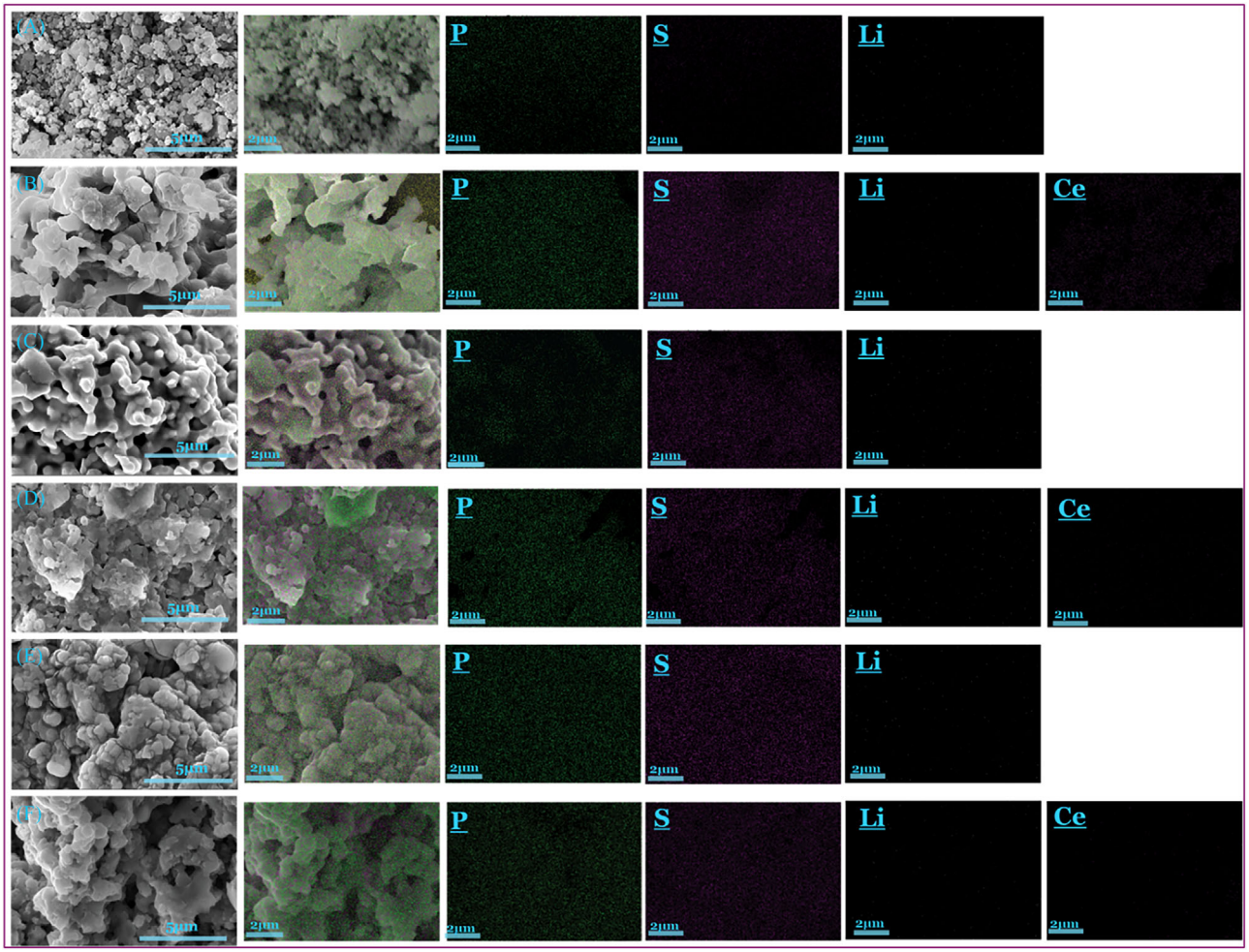

FIGURE 6 SEM images and energy dispersive X-ray spectroscopy elemental mapping of (A) $Li_7P_3S_{11}$ after heating to 250°C; (B) $Li_7P_{2.9}Ce_{0.1}S_{11}$ after heating to 250°C; (C) $Li_7P_3S_{11}$ after heating to 275°C; (D) $Li_7P_{2.9}Ce_{0.1}S_{11}$ after heating to 275°C; (E) $Li_7P_3S_{11}$ after heating to 300°C; (F) $Li_7P_{2.9}Ce_{0.1}S_{11}$ after heating to 300°C.

TABLE 2 Total resistance and ionic conductivity of pristine $Li_7P_3S_{11}$ and Ce_2S_3 doped $Li_7P_3S_{11}$ glass-ceramic.

	Temperature (°C)	Total resistance	Ionic conductivity (S cm^{-1})
$Li_7P_3S_{11}$	250	634.4	6.37×10^{-5}
	275	355.7	1.13×10^{-4}
	300	231.5	1.74×10^{-4}
	325	128	3.15×10^{-4}
	350	171	2.36×10^{-4}
$Li_7P_3S_{11}$+Ce_2S_3		**250**	
	1 wt%	52.4	7.7×10^{-4}
	3 wt%	59.9	6.75×10^{-4}
	5 wt%	73.6	5.49×10^{-4}
		275	
	1 wt%	64.7	6.3×10^{-4}
		300	
	1 wt%	130.7	3.1×10^{-4}

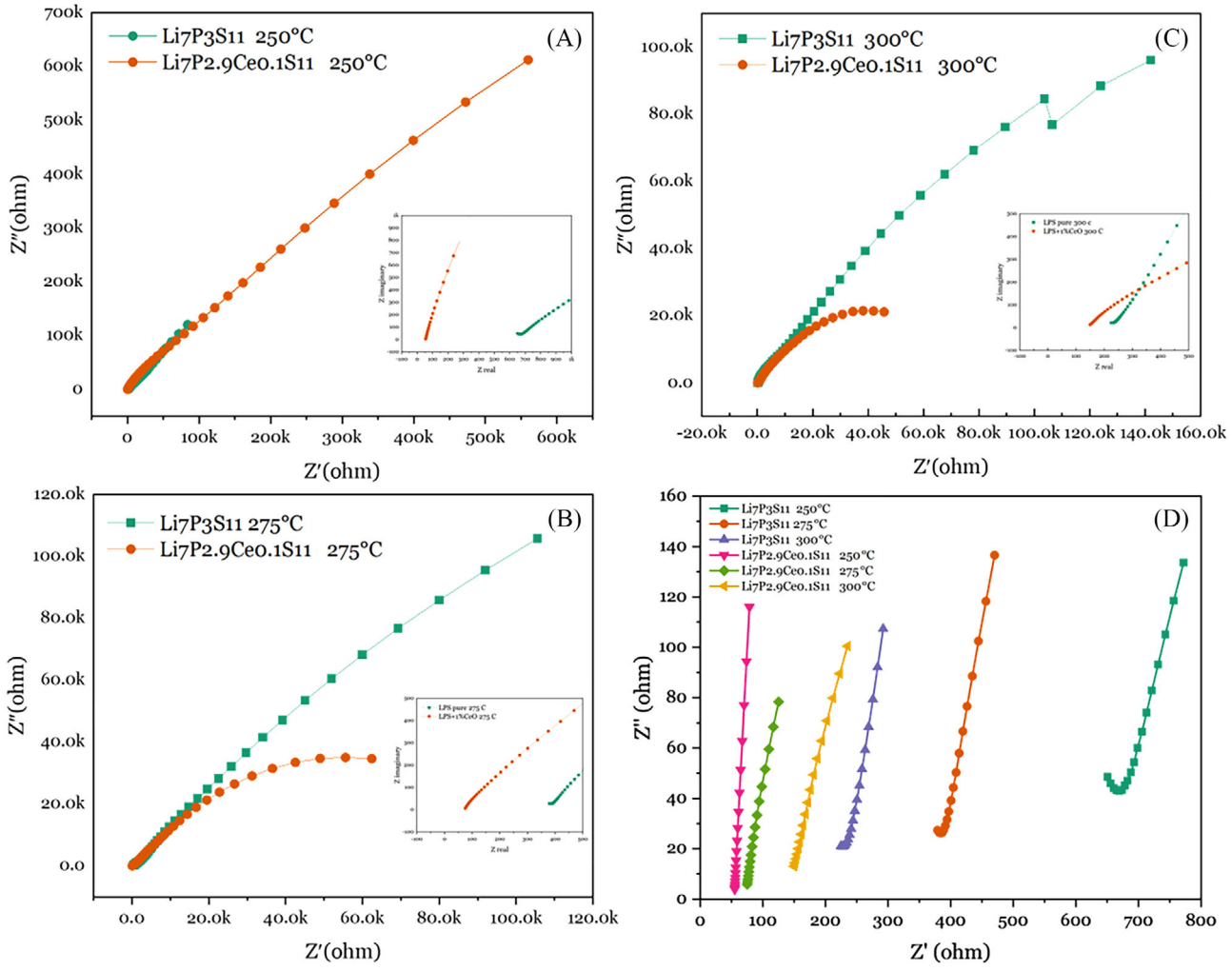

FIGURE 7 The impedance spectra of (A) pristine $Li_7P_3S_{11}$ and $Li_7P_{2.9}Ce_{0.1}S_{11}$ glass-ceramic after heating to 250°C; (B) pristine $Li_7P_3S_{11}$ and $Li_7P_{2.9}Ce_{0.1}S_{11}$ glass-ceramic after heating to 275°C; (C) pristine $Li_7P_3S_{11}$ and $Li_7P_{2.9}Ce_{0.1}S_{11}$ glass-ceramic after heating to 300°C; (D) a zoomed-in view of impedance spectra for all samples.

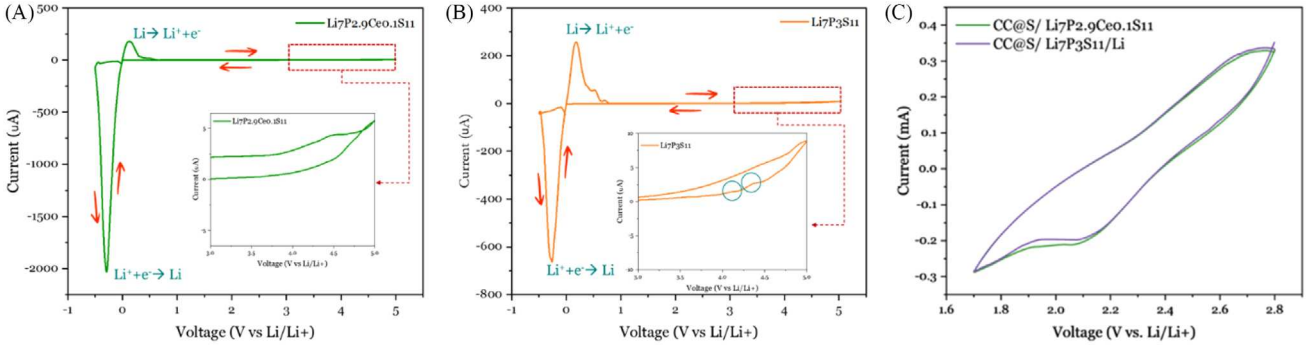

FIGURE 8 Comparison of cyclic voltammetry (CV) curves for Li/solid electrolyte/stainless steel batteries with two different glass-ceramic electrolyte compositions: (A) $Li_7P_{2.9}Ce_{0.1}S_{11}$ and (B) $Li_7P_3S_{11}$. The curves were obtained through CV at a scanning rate of 1 $mV{\cdot}s^{-1}$, spanning a potential range from −0.5 to 5 V (vs. Li/Li^+) at 25°C. (C) CV measurements of CC@S/$Li_7P_{2.9}Ce_{0.1}S_{11}$/Li and CC@S/$Li_7P_3S_{11}$/Li within 1.6 – 2.8 V at a scan rate of 0.5 mV/s.

rate of 1 $mV{\cdot}s^{-1}$, encompassing a potential range from 0.5 to 5 V (vs. Li/Li^+). Upon analyzing the CV curves, several key observations emerge. Both the $Li_7P_3S_{11}$ and $Li_7P_{2.9}Ce_{0.1}S_{11}$ electrolytes exhibit a wide electrochemical window, extending up to 5 V. However, the $Li_7P_{2.9}Ce_{0.1}S_{11}$ electrolyte demonstrates considerably better electrochemical stability, compared to $Li_7P_3S_{11}$. Further examination of Figure 8A,B reveals that the CV curve for $Li_7P_3S_{11}$ displays larger fluctuations between 4 and 5 V, suggesting some slight instability arising from side reactions at the interface between $Li_7P_3S_{11}$ and the lithium metal. In contrast, the $Li_7P_{2.9}Ce_{0.1}S_{11}$ electrolyte demonstrates almost complete compatibility with the lithium electrode, indicating enhanced stability. Additionally, both samples exhibit distinct peaks in the CV curves. Just below 0 V, there is a peak associated with lithium deposition ($Li^+ + e^- \rightarrow Li$), while at 0.17 V, a peak corresponding to the dissolution process ($Li \rightarrow Li^+ + e^-$) can be observed. These findings align with previous literature on sulfide electrolytes, where similar CV curve behavior has been reported.[38,40,60,61]

Comparisons are made between the CV properties of carbon cloth (CC)@S/$Li_7P_{2.9}Ce_{0.1}S_{11}$/Li and CC@S/$Li_7P_3S_{11}$/Li batteries (Figure 8C). In both cases, oxidation and reduction peaks are observed at 2.7 and 1.9 V, respectively. The presence of symmetrical pairs of oxidation and reduction peaks indicates a well-reversible Li^+ ion intercalation–deintercalation process. It is evident that the all solid- state Li- S battery (ASSLSB) with the CC@S cathode and the $Li_7P_{2.9}Ce_{0.1}S_{11}$ solid-state electrolyte exhibits higher capacitance performance, compared to the $Li_7P_3S_{11}$ electrolyte. Consequently, the CC@S/$Li_7P_{2.9}Ce_{0.1}S_{11}$/Li battery demonstrates lower internal resistance, leading to higher specific capacitance and improved power performance.[62–64]

4 | CONCLUSION

To summarize, the production of glass-ceramic electrolytes based on Li_2S-P_2S_5 (LPS) can be achieved by incorporating 1 wt%, 3 wt%, or 5 wt% of Ce_2S_3 through a straightforward wet-chemical technique involving acetonitrile and subsequent annealing. The study investigated the crystal structure, ionic conductivity, and chemical stability of $Li_7P_3S_{11}$ glass-ceramic electrolytes across a range of temperatures (250–350°C). The findings revealed a turning point at 325°C, where the ionic conductivity of pure (undoped) $Li_7P_3S_{11}$ began to decline. The highest ionic conductivity, reaching 3.15×10^{-4} S cm^{-1}, was achieved at this temperature for pure (undoped) $Li_7P_3S_{11}$. Through the addition of 1 wt% Ce_2S_3 and subjecting the material to a heat treatment at 250°C, the glass-ceramic electrolyte displayed a remarkable ionic conductivity of 7.7×10^{-4} S cm^{-1} at 25°C. Additionally, it demonstrated a consistent and wide electrochemical potential range, extending up to 5 volts, compared to the Li/Li^+ reference electrode. The addition of Ce_2S_3 enhances the thermal stability of $Li_7P_3S_{11}$ during heating by affecting the glass transition and crystallization temperature during the heating process. The Raman and XPS analyses indicate that Ce_2S_3 inhibits the decomposition of the $P_2S_7^{4-}$ (with high ionic conductivity) to PS_4^{3-} and $P_2S_6^{4-}$. Electron microscopy analysis also suggests that doped LPS has a greater crystallinity than pure LPS. In view of this, $Li_7P_{2.9}Ce_{0.1}S_{11}$ electrolyte has a high potential for use as a solid-state electrolyte in the construction of high-performance all-solid-state Li-S batteries.

ACKNOWLEDGMENTS

This work is supported by the National Science Foundation (CBET-2118784 and TI-2147564). This project also receives partial financial support from the Alabama Transportation Institute and Alabama Water Institute. The use of electron microscopy facilities at the Alabama Analytical Research Center (AARC), The University of Alabama, is gratefully acknowledged. We thank Zhen Wei and Sakibul Azam for providing valuable technical support and suggestions during the electrochemical tests.

CONFLICT OF INTEREST STATEMENT

There are no competing financial interests or personal relationships influencing the authors' work.

ORCID

Ruigang Wang https://orcid.org/0000-0002-0678-7460

REFERENCES

1. Liang Y, Wei Z, Wang H-E, Wang R, Zhang X. Flexible freestanding conductive nanopaper based on PPy: PSS nanocellulose composite for supercapacitors with high performance. Sci China Mater. 2023;66(3):964–73.
2. Liang Y, Wei Z, Wang H-E, Flores M, Wang R, Zhang X. Flexible and freestanding PANI: PSS/CNF nanopaper electrodes with enhanced electrochemical performance for supercapacitors. J Power Sources. 2022;548:232071.
3. Wei Z, Li J, Wang Y, Wang R. High-performance Li-S batteries enabled by polysulfide-infiltrated free-standing 3D carbon cloth with CeO_2 nanorods decoration. Electrochim Acta. 2021;388:138645.
4. Lewis NS, Nocera DG. Powering the planet: chemical challenges in solar energy utilization. Proc Natl Acad Sci. 2006;103(43):15729–35.
5. Schaefer JF, Lu Y, Moganty SS, Agarwal P, Jayaprakash N, Archer LA. Electrolytes for high-energy lithium batteries. Appl Nanosci. 2012;2:91–109.
6. Ud Din MM, Ramakumar S, Santhakumari IM, Murugan R. Advances in electrolytes for high capacity rechargeable lithium-sulphur batteries. Current Smart Mater. 2021;5(1):3–37.

7. Ahasan MR, Hossain M, Ding X, Wang R. Non-equilibrium plasma-assisted dry reforming of methane over shape-controlled CeO_2 supported ruthenium catalysts. J Mater Chem A. 2023;11:10993–1009.
8. Ranganathan RV, Jony B, Fondriest SM, Liu Z, Wang R, Uddi M. Plasma-catalysis chemical looping CH_4 reforming with water splitting using ceria supported Ni based La-perovskite nano-catalyst. J CO2 Util. 2019;32:11–20.
9. Liu J, Bao Z, Cui Y, Dufek EJ, Goodenough JB, Khalifah P, et al. Pathways for practical high-energy long-cycling lithium metal batteries. Nat Energy. 2019;4(3):180–86.
10. Manthiram A, Yu X, Wang S. Lithium battery chemistries enabled by solid-state electrolytes. Nat Rev Mater. 2017;2(4):1–16.
11. Zhou J, Liu X, Zhu L, Zhou J, Guan Y, Chen L, et al. Deciphering the modulation essence of p bands in Co-based compounds on Li-S chemistry. Joule. 2018;2(12):2681–93.
12. Chen S, Niu C, Lee H, Li Q, Yu L, Xu W, et al. Critical parameters for evaluating coin cells and pouch cells of rechargeable Li-metal batteries. Joule. 2019;3(4):1094–105.
13. Wang Y, Richards WD, Ong SP, Miara LJ, Kim JC, Mo Y, et al. Design principles for solid-state lithium superionic conductors. Nat Mater. 2015;14(10):1026–31.
14. Jia H, Zou L, Gao P, Cao X, Zhao W, He Y, et al. High-performance silicon anodes enabled by nonflammable localized high-concentration electrolytes. Adv Energy Mater. 2019;9(31):1900784.
15. Li J, Liu Z, Ma W, Dong H, Zhang K, Wang R. Low-temperature synthesis of cubic phase $Li_7La_3Zr_2O_{12}$ via sol-gel and ball milling induced phase transition. J Power Sources. 2019;412:189–96.
16. Li J, Wang R. Recent advances in the interfacial stability, design and in situ characterization of garnet-type $Li_7La_3Zr2O_{12}$ solid-state electrolytes based lithium metal batteries. Ceram Int. 2021;47(10):13280–90.
17. Sun C, Liu J, Gong Y, Wilkinson DP, Zhang J. Recent advances in all-solid-state rechargeable lithium batteries. Nano Energy. 2017;33:363–86.
18. Yu T, Yang X, Yang R, Bai X, Xu G, Zhao S, et al. Progress and perspectives on typical inorganic solid-state electrolytes. J Alloys Compd. 2021;885:161013.
19. Kato Y, Hori S, Kanno R. $Li_{10}GeP_2S_{12}$-type superionic conductors: synthesis, structure, and ionic transportation. Adv Energy Mater. 2020;10(42):2002153.
20. Wang H, Cao X, Liu W, Sun X. Research progress of the solid state lithium-sulfur batteries. Front Energy Res. 2019;7:112.
21. Lei D, Shi K, Ye H, Wan Z, Wang Y, Shen L, et al. Progress and perspective of solid-state lithium–sulfur batteries. Adv Funct Mater. 2018;28(38):1707570.
22. Lv F, Wang Z, Shi L, Zhu J, Edström K, Mindemark J, et al. Challenges and development of composite solid-state electrolytes for high-performance lithium ion batteries. J Power Sources. 2019;441:227175.
23. Hikima K, Kusaba I, Gamo H, Phuc NHH, Muto H, Matsuda A. High ionic conductivity with improved lithium stability of CaS- and CaI_2-doped $Li_7P_3S_{11}$ solid electrolytes synthesized by liquid-phase synthesis. ACS Omega. 2022;7:16561–67.
24. Zhang J, Huang L, Gu X. Failure mechanism of solid-state electrolyte $Li_{10}GeP_2S_{12}$ in a moist atmosphere: a first-principles study. Mater Adv. 2022;3(7):3143–50.
25. Viallet V, Seznec V, Hayashi A, Tatsumisago M, Pradel A. Glasses and glass-ceramics for solid-state battery applications-Chapter 50. In: Musgraves JD, Hu J, Calvez L, editors. Springer handbook of glass. Cham: Springer; 2019. p. 1707–64.
26. Li S, Zhang SQ, Shen L, Liu Q, Ma JB, Lv W, et al. Progress and perspective of ceramic/polymer composite solid electrolytes for lithium batteries. Adv Sci. 2020;7(5):1903088.
27. Chang D, Oh K, Kim SJ, Kang K. Super-ionic conduction in solid-state $Li_7P_3S_{11}$-type sulfide electrolytes. Chem Mater. 2018;30(24):8764–70.
28. Zhou J, Chen P, Wang W, Zhang X. $Li_7P_3S_{11}$ electrolyte for all-solid-state lithium-ion batteries: structure, synthesis, and applications. Chem Eng J. 2022;446:137041.
29. Tufail MK, Ahmad N, Yang L, Zhou L, Naseer MA, Chen R, et al. A panoramic view of $Li_7P_3S_{11}$ solid electrolytes synthesis, structural aspects and practical challenges for all-solid-state lithium batteries. Chin J Chem Eng. 2021;39:16–36.
30. Mizuno F, Hayashi A, Tadanaga K, Tatsumisago M. New lithium-ion conducting crystal obtained by crystallization of the Li_2S–P_2S_5 glasses. Electrochem Solid-State Lett. 2005;8(11):A603.
31. Yamane H, Shibata M, Shimane Y, Junke T, Seino Y, Adams S, et al. Crystal structure of a superionic conductor, $Li_7P_3S_{11}$. Solid State Ionics. 2007;178(15-18):1163–67.
32. Arinicheva Y, Wolff M, Lobe S, Dellen C, Fattakhova-Rohlfing D, Guillon O, et al. Ceramics for electrochemical storage. In: Guillon O, editor. Advanced ceramics for energy conversion and storage. Amsterdam: Elsevier; 2020. p. 549–709.
33. Miura A, Rosero-Navarro NC, Sakuda A, Tadanaga K, Phuc NH, Matsuda A, et al. Liquid-phase syntheses of sulfide electrolytes for all-solid-state lithium battery. Nat Rev Chem. 2019;3(3):189–98.
34. Gamo H, Nagai A, Matsuda A. The effect of solvent on reactivity of the Li_2S–P_2S_5 system in liquid-phase synthesis of $Li_7P_3S_{11}$ solid electrolyte. Sci Rep. 2021;11(1):21097.
35. Busche MR, Weber DA, Schneider Y, Dietrich C, Wenzel S, Leichtweiss T, et al. In situ monitoring of fast Li-ion conductor $Li_7P_3S_{11}$ crystallization inside a hot-press setup. Chem Mater. 2016;28(17):6152–65.
36. Jung S-Y, Rajagopal R, Ryu K-S. Synthesis and electrochemical performance of (100−x) $Li_7P_3S_{11}$-xLi_2OHBr composite solid electrolyte for all-solid-state lithium batteries. J Energy Chem. 2020;47:307–16.
37. Song R, Xu R, Wang Z, Yang M, Yan X, Yu C, et al. Oxide doping improving interface performance for $Li_7P_3S_{11}$ solid electrolytes. J Alloys Compd. 2022;921:166125.
38. Wu Z, Xie Z, Yoshida A, An X, Wang Z, Hao X, et al. Novel SeS_2 doped Li_2S-P_2S_5 solid electrolyte with high ionic conductivity for all-solid-state lithium sulfur batteries. Chem Eng J. 2020;380:122419.
39. Ge Q, Zhou L, Lian Y-M, Zhang X, Chen R, Yang W. Metal-phosphide-doped $Li_7P_3S_{11}$ glass-ceramic electrolyte with high ionic conductivity for all-solid-state lithium-sulfur batteries. Electrochem Commun. 2018;97:100–104.
40. Xu R-C, Xia X-H, Wang X-L, Xia Y, Tu J-P. Tailored Li_2S–P_2S_5 glass-ceramic electrolyte by MoS_2 doping, possessing high ionic

conductivity for all-solid-state lithium-sulfur batteries. J Mater Chem A. 2017;5(6):2829–34.
41. Li Y, Li J, Cheng J, Xu X, Chen L, Ci L. Enhanced air and electrochemical stability of $Li_7P_3S_{11}$–based solid electrolytes enabled by aliovalent substitution of SnO_2. Adv Mater Interfaces. 2021;8(14):2100368.
42. Minami K, Hayashi A, Ujiie S, Tatsumisago M. Electrical and electrochemical properties of glass–ceramic electrolytes in the systems Li_2S–P_2S_5–P_2S_3 and Li_2S–P_2S_5–P_2O_5. Solid State Ionics. 2011;192(1):122–25.
43. Xu X, Wang L, Fei H, Ci L. Boron nitride doped $Li_7P_3S_{11}$ solid electrolyte with improved interfacial compatibility and application in all-solid-state Li/S battery. J Mater Sci: Mater Electron. 2019;30:19119–25.
44. Yu P, Ahmad N, Zeng C, Lv L, Dong Q, Yang W. Tailored $Li_7P_3S_{11}$ electrolyte by In_2S_3 doping suppresses electrochemical decomposition for high-performance all-solid-state lithium–sulfur batteries. ACS Appl Energy Mater. 2022;5(11):13429–38.
45. Azam S, Wei Z, Wang R. Cerium oxide nanorods anchored on carbon nanofibers derived from cellulose paper as effective interlayer for lithium sulfur battery. J Colloid Interface Sci. 2022;615:417–31.
46. Azam S, Wei Z, Wang R. Adsorption-catalysis design with cerium oxide nanorods supported nickel-cobalt-oxide with multifunctional reaction interfaces for anchoring polysulfides and accelerating redox reactions in lithium sulfur battery. J Colloid Interface Sci. 2023;635:466–80.
47. Wei Z, Wang R. Chemically etched CeO_{2-x} nanorods with abundant surface defects as effective cathode additive for trapping lithium polysulfides in Li-S batteries. J Colloid Interface Sci. 2022;615:527–42.
48. Zhou L, Tufail MK, Ahmad N, Song T, Chen R, Yang W. Strong interfacial adhesion between the Li_2S cathode and a functional $Li_7P_{2.9}Ce_{0.2}S_{10.9}Cl_{0.3}$ solid-state electrolyte endowed long-term cycle stability to all-solid-state lithium–sulfur batteries. ACS Appl Mater Interfaces. 2021;13(24):28270–80.
49. Ahasan MR, Hossain MM, Ding X, Wang R. Non-equilibrium plasma-assisted dry reforming of methane over shape-controlled CeO_2 supported ruthenium catalysts. J Mater Chem A. 2023;11(20):10993–1009.
50. Minami T, Hayashi A, Tatsumisago M. Recent progress of glass and glass-ceramics as solid electrolytes for lithium secondary batteries. Solid State Ionics. 2006;177(26-32):2715–20.
51. Calpa M, Rosero-Navarro NC, Miura A, Tadanaga K. Preparation of sulfide solid electrolytes in the Li_2S–P_2S_5 system by a liquid phase process. Inor Chem Front. 2018;5(2):501–8.
52. Zheng J, Elgin J, Shao J, Wu Y. Differentiating grain and grain boundary ionic conductivities of Li-ion antiperovskite electrolytes. eScience. 2022;2(6):639–45.
53. Dube D, Saraswat A. Grain boundary effects on ionic conductivity of superionic conductors. J Appl Phys. 1982;53(10):7095–96.
54. Rangasamy E, Liu Z, Gobet M, Pilar K, Sahu G, Zhou W, et al. An iodide-based $Li_7P_2S_8I$ superionic conductor. J Am Chem Soc. 2015;137(4):1384–87.
55. Wang Y, Lu D, Bowden M, El Khoury PZ, Han KS, Deng ZD, et al. Mechanism of formation of $Li_7P_3S_{11}$ solid electrolytes through liquid phase synthesis. Chem Mater. 2018;30(3):990–97.
56. Wenzel S, Weber DA, Leichtweiss T, Busche MR, Sann J, Janek J. Interphase formation and degradation of charge transfer kinetics between a lithium metal anode and highly crystalline $Li_7P_3S_{11}$ solid electrolyte. Solid State Ionics. 2016;286:24–33.
57. Tufail MK, Ahmad N, Zhou L, Faheem M, Yang L, Chen R, et al. Insight on air-induced degradation mechanism of $Li_7P_3S_{11}$ to design a chemical-stable solid electrolyte with high Li_2S utilization in all-solid-state Li/S batteries. Chem Eng J. 2021;425:130535.
58. Jung WD, Yun B-N, Jung H-G, Choi S, Son J-W, Lee J-H, et al. Configuring PS_x tetrahedral clusters in Li-excess $Li_7P_3S_{11}$ solid electrolyte. APL Mater. 2018;6(4):047902.
59. Ito S, Nakakita M, Aihara Y, Uehara T, Machida N. A synthesis of crystalline $Li_7P_3S_{11}$ solid electrolyte from 1, 2-dimethoxyethane solvent. J Power Sources. 2014;271:342–45.
60. Hayashi A, Muramatsu H, Ohtomo T, Hama S, Tatsumisago M. Improvement of chemical stability of Li_3PS_4 glass electrolytes by adding M_xO_y(M = Fe, Zn, and Bi) nanoparticles. J Mater Chem A. 2013;1(21):6320–26.
61. Wang H, Hood ZD, Xia Y, Liang C. Fabrication of ultrathin solid electrolyte membranes of β-Li_3 PS_4 nanoflakes by evaporation-induced self-assembly for all-solid-state batteries. J Mater Chem A. 2016;4(21):8091–96.
62. Yang X, Zhang F, Zhang L, Zhang T, Huang Y, Chen Y. A high-performance graphene oxide-doped ion gel as gel polymer electrolyte for all-solid-state supercapacitor applications. Adv Funct Mater. 2013;23(26):3353–60.
63. Han F, Gao T, Zhu Y, Gaskell KJ, Wang C. A battery made from a single material. Adv Mater. 2015;27(23):3473–83.
64. Zhang W, Leichtweiß T, Culver SP, Koerver R, Das D, Weber DA, et al. The detrimental effects of carbon additives in $Li_{10}GeP_2S_{12}$-based solid-state batteries. ACS Appl Mater Interfaces. 2017;9(41):35888–96.

SUPPORTING INFORMATION

Additional supporting information can be found online in the Supporting Information section at the end of this article.

How to cite this article: Mirtaleb A, Wang R. A highly stable and conductive cerium-doped $Li_7P_3S_{11}$ glass-ceramic electrolyte for solid-state lithium–sulfur batteries. J Am Ceram Soc. 2024;107:3800–3812.
https://doi.org/10.1111/jace.19712